Research Paper

Facile synthesis of ternary TiO$_2$ NP/Rh & Sb-codoped TiO$_2$ NR/titanate NT composites photocatalyst: Simultaneous removals of Cd^{2+} ions and Orange (II) dye under visible light irradiation ($\lambda \geq 420$ nm)

Su-Gyeong Kim[a,1], Love Kumar Dhandole[a,1], Jeong-Muk Lim[a], Weon-Sik Chae[b], Hee-Suk Chung[c], Byung-Taek Oh[a], Jum Suk Jang[a,*]

[a] Division of Biotechnology, Safety, Environment and Life Science Institute, College of Environmental and Bioresource Sciences, Chonbuk National University, Iksan 570-752, Republic of Korea
[b] Daegu Center, Korea Basic Science Institute, Daegu 41566, Republic of Korea
[c] Analytical Research Division, Korea Basic Science Institute, Jeonju, Jeollabuk-do, 54907, Republic of Korea

ARTICLE INFO

ABSTRACT

In this study, rhodium and antimony doped nanorod (RS-TONR) was prepared by a molten salt solid state chemical reaction, and TiO$_2$ nanorod and titanate nanotube (RS-TONR/TiNT) composite photocatalyst was synthesized by a hydrothermal method for different reaction times. The structural and chemical analyses of nanomaterials were performed by FE-SEM, XRD, UV-DRS and surface BET characterizations. The XRD and HR-TEM data confirmed that the as-synthesized material had mixed phase of TiO$_2$ nanorod and Titanate nanotube (RS-TONR/TiNT). The photocatalytic activity of the composite photocatalyst was observed over the degradation of Orange (II) dye under visible light irradiation. Acid treatment and copper loading was conducted to enhance the surface property of RS-TONR/TiNT sample. The formation of TiO$_2$ nanoparticle with anatase phase was observed by TEM and XRD analysis. The TEM mapping data also confirmed that copper oxide nanoparticles were well dispersed on the surface of titanate nanotubes. These dispersed nanoparticles were observed by XPS and STEM characterizations. The higher removal efficiency of Cd^{2+} ions was observed over the acid treated and untreated Cu3-TNP/TiNT/RS-TONR in the presence of Orange (II) dye. A higher photocatalytic activity of acid treated and Cu3-TNP/TiNT/RS-TONR was simultaneously obtained in the presence of cadmium ions during the degradation of Orange (II) dye.

1. Introduction

The well-known abundant titanium oxide is considered an important and promising photocatalyst in the research field, because of its wide band gap, nontoxicity, low cost and chemical stability [1]. However, the photocatalytic activity of TiO$_2$ is limited, due to its wide band gap property of absorbance only in short wavelength. Recently, several studies have shown that metal doping into the TiO$_2$ lattice can enhance the performance by reducing its existing band gap with the introduction of new dopant energy levels. This new energy level can decrease the recombination rate and shift the absorption wavelength towards the visible light region [2,3].

Several studies have reported that rhodium-doped TiO$_2$ has good absorbance under the visible light region [4]. Moreover, the photocatalytic activity of rhodium-doped TiO$_2$ is hindered by rhodium

intermediate Rh^{4+} species [5,6]. Niishiro et al. have reported that antimony (pentavalent dopant) co-dopant enhanced the photocatalytic activities by compensation of the rhodium species [6]. Further, study has confirmed that rhodium and antimony co-doped TiO$_2$ has low bang-gap energy and good photocatalytic performance under visible light irradiation [5].

The reduced band gap is not only the sufficient to enhance the photocatalytic performance. Charge recombination factor is a challenging task to harvest the high photocatalytic activity. There are several studies has shown the approach to reduce the charge recombination rate. Hou et al. studied the effect of Cu$_2$O nanoparticles loaded TiO$_2$ nanotube arrays, the improved photoelectrocatalytic activity attributes to the synergism of Cu$_2$O nanoparticles and TiO$_2$ nanotubes arrays [7]. This Cu$_2$O nanoparticle could reduce the recombination of electron−-hole by sending the electrons to the conduction band of TiO$_2$ nanotubes
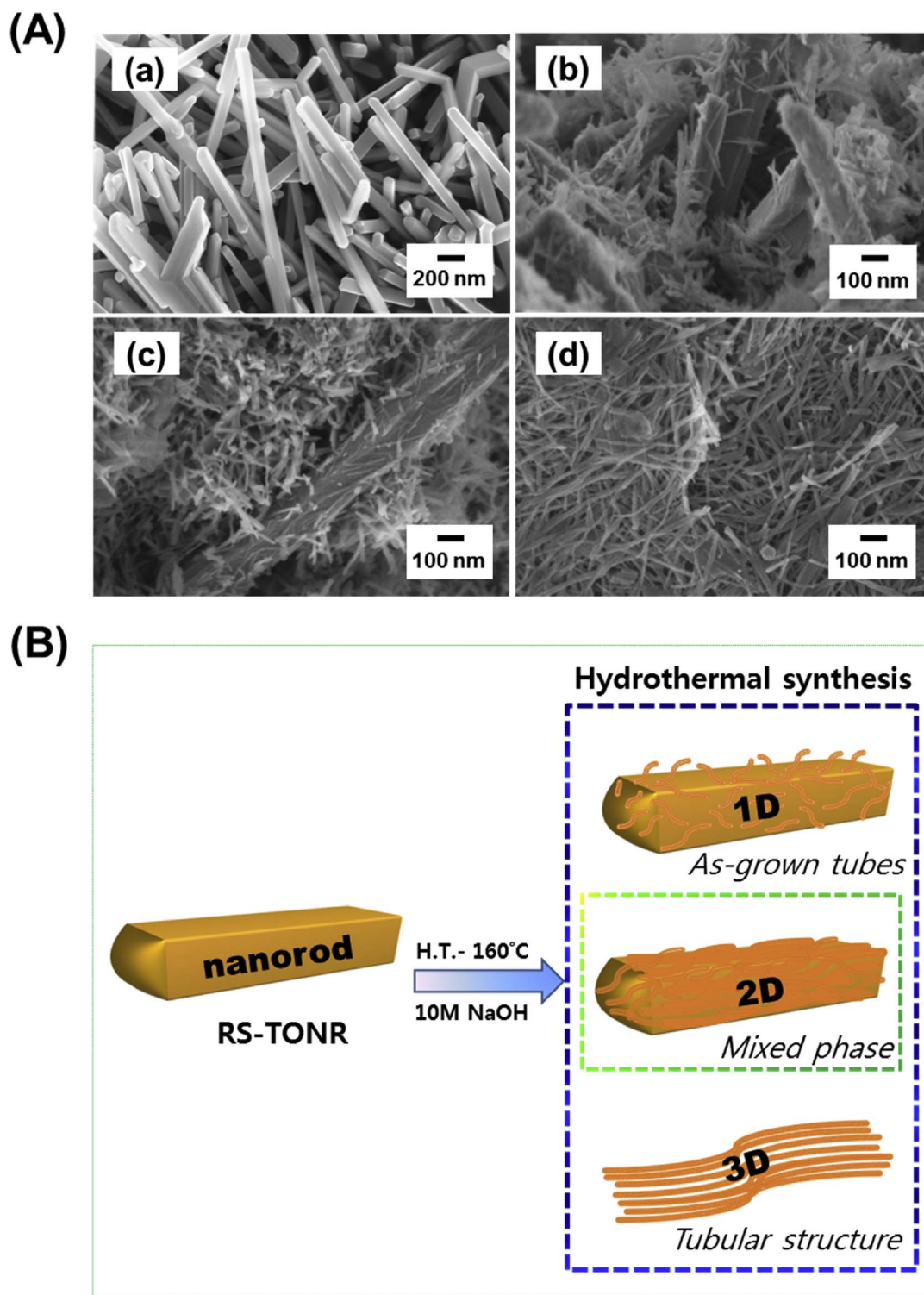
Fig. 1. (A) FE-SEM images of (a) RS-TONRs, (b) RS-TONR/TiNT-1D, (c) RS-TONR/TiNT-2D, and (d) RS-TONR/TiNT-3D; and (B) Diagram of the formation mechanism of titanate nanostructures corresponding to their morphologies.

and enhanced the decomposition of 4-chlorophenol by oxidization. The surface charge recombination is a big concern in heterojunction composite materials. A high effectively approach of n-types CuInS$_2$ modified TiO$_2$ nanotubes heterojunction enhance the visible-light activity of TiO$_2$ NTs electrode and the n–n heterojunction structure could favor the surface-interface charge separation and transfer followed by dramatic suppression of the electron–hole recombination [8]. The similar approach of lowing the electron-hole recombination rate was well

demonstrated by Liu et al. where Mn$_{0.5}$Fe$_2$O$_4$ nanoparticles deposited TiO$_2$ nanotube arrays shows the high photoelectrocatalytic performance in the degradation of 2,4-DCP [9].

Present study has focused on the synthesis of visible light active composite (mixture of titanate and co-doped nanorods) material by using rhodium-antimony co-doped TiO$_2$ nanorod as the precursor during hydrothermal synthesis. Titanate nanotube has large specific surface area, high length–diameter aspect ratio, special interlayered
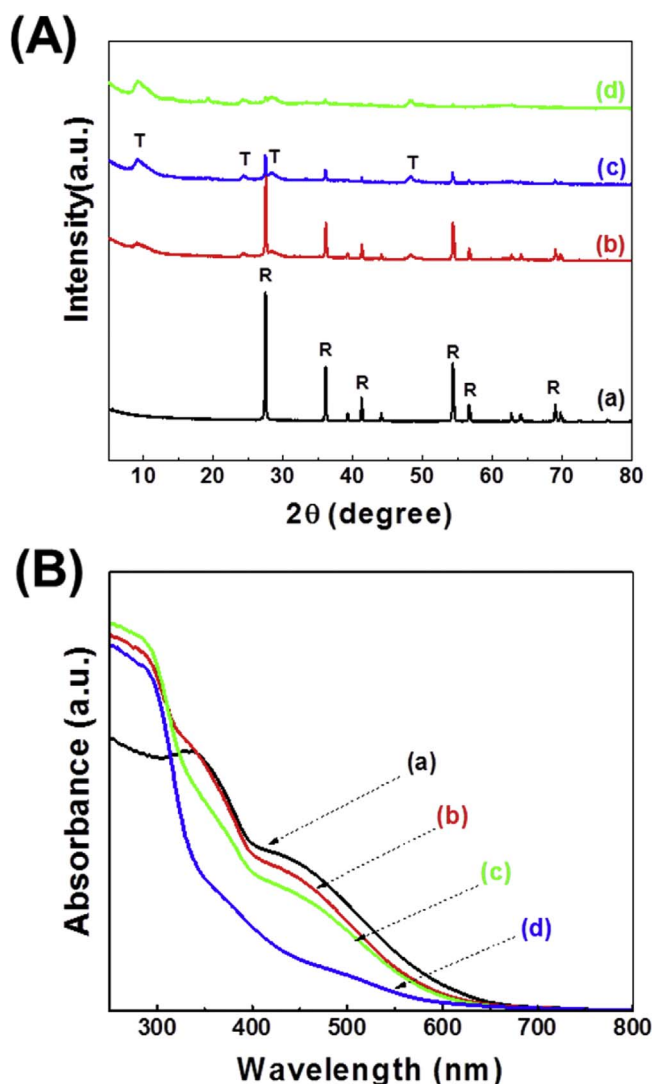
Fig. 2. XRD patterns (A) of (a) RS-TONRs, (b) RS-TONR/TiNT-1D, (c) RS-TONR/TiNT-2D and (d) RS-TONR/TiNT-3D (R: rutile, T: titanate) and UV–vis DRS spectrum; and (B) of 25 μM orange(II) dye under 420 nm visible light for (a) RS-TONRs, (b) RS-TONR/TiNT-1D, (c) RS-TONR/TiNT-2D, and (d) RS-TONR/TiNT-3D.

Fig. 3. (A) The photo degradation of 25 μM Orange (II) dye under 420 nm visible light for (a) RS-TONRs, (b) RS-TONR/TiNT-1D, (c) RS-TONR/TiNT-2D, (d) RS-TONR/TiNT-3D, and (a') RS-TONRs-1M, (b') RS-TONR/TiNT-1D-1M, (c') RS-TONR/TiNT-2D-1M, and (d') RS-TONR/TiNT-3D-1M; and (B) Diagram of the mechanism for RS-TONR/TiNT-2D-1M.

titanate structure and good ion–exchange properties [10–12]. These properties of titanate make more efficient adsorbent that leads to removal of heavy metal ions and ionic organic pollutants. [10,13] The advantages of this composite material are rutile rhodium-antimony co-doped TiO₂ nanorods have higher bandgap energy over the titanate nanotubes which can supports the charge transfer mechanism, [14] visible active material and photocatalytic property. Therefore, as TNTs are derived from TiO₂, it can expect that it could be applicable in photocatalytic activity. These overall properties of co-doping NRs and titanate nanostructure have attracted research interest in its environmental applications, such as the removal of heavy metal ions and organic pollutants [15].

Over the last few decades, a large amount of wastewater that contains different kinds of pollutants has been discharged directly into fresh water bodies. This practice causes toxicity to aquatic, and marine life, and harmful effects on human health [16,17]. These pollutants are broadly classified as heavy metal ions (Co^{2+}, Ni^{2+}, Cr^{3+}, and Fe^{3+}), toxic metal ions (Cd^{2+}, Pb^{2+}, and As^{2+}), and dye effluents [11,18–22]. Dye wastewater has presented serious problems worldwide, because of its huge volume of production, chemical stability, and constituent contaminants, which include acids, bases, dissolved solids, and toxic compounds [23,24]. Heavy metal cadmium (Cd) is released into the
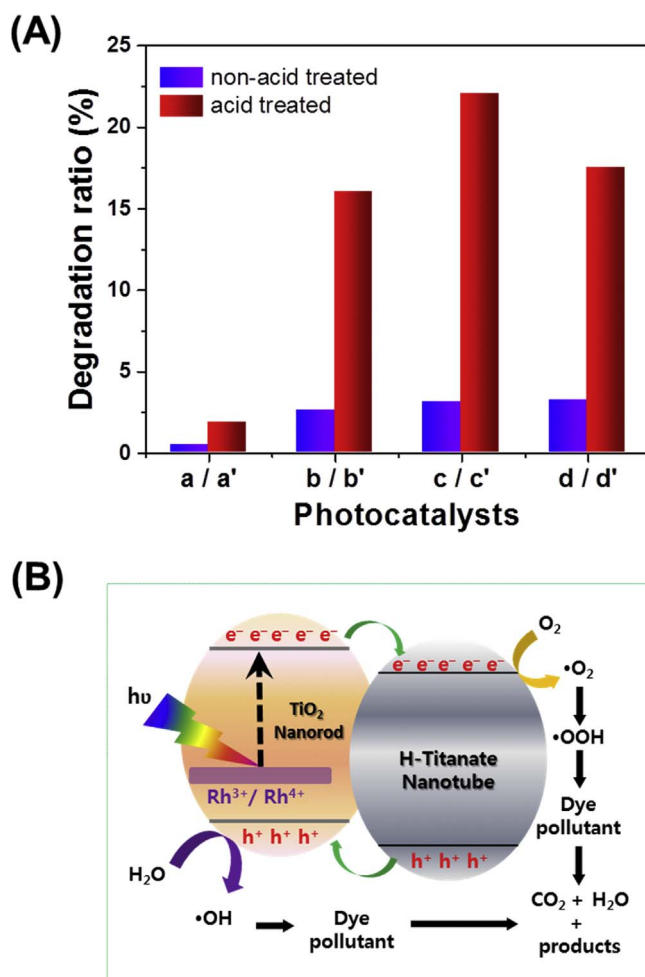
environment from various sources, such as mining, alloy metallurgy, waste streams of electroplating, smelting, pigments and plastic industries, battery, and refining processes [25–27]. Cadmium has been well recognized for its negative effect on the environment, where it accumulates readily in eco-systems, and carcinogen leads to disease, such as lung, kidney, and prostate cancer for human, due to prolonged exposure [28,29].

Recently, several studies have shown separative strategies for dye pollutants and heavy and toxic metal ions removal applications. The combined *in situ* approach for removal of both targeted pollutants is more advantageous from an environmental aspect. During our study, this key point was acknowledged to design the appropriate material for simultaneous removal of dye and cadmium ions. Recently, Liu et al. reported high photocatalytic and adsorptive performance by titanate nanotubes and anatase TiO₂ over organic pollutants and heavy metals under UV light. To improve their photocatalytic performance, titanate nanotube and TiO₂ with anatase phase were modified while retaining their adsorptive property [15]. Doong et al. enhanced the photocatalytic activity of Cu-deposited titanate nanotube that applied to effective degradation of toxic chemicals in aqueous solutions, but this material still works under UV light [30]. Lee et al. studied the application of titanate nanotubes for the adsorptive removal of dyes, where modified titanate nanotubes showed high removal efficiency over dye pollutants [22].

In this study, rhodium and antimony doped nanorod (RS-TONRs) was prepared by a molten salt solid state chemical reaction, while TiO₂
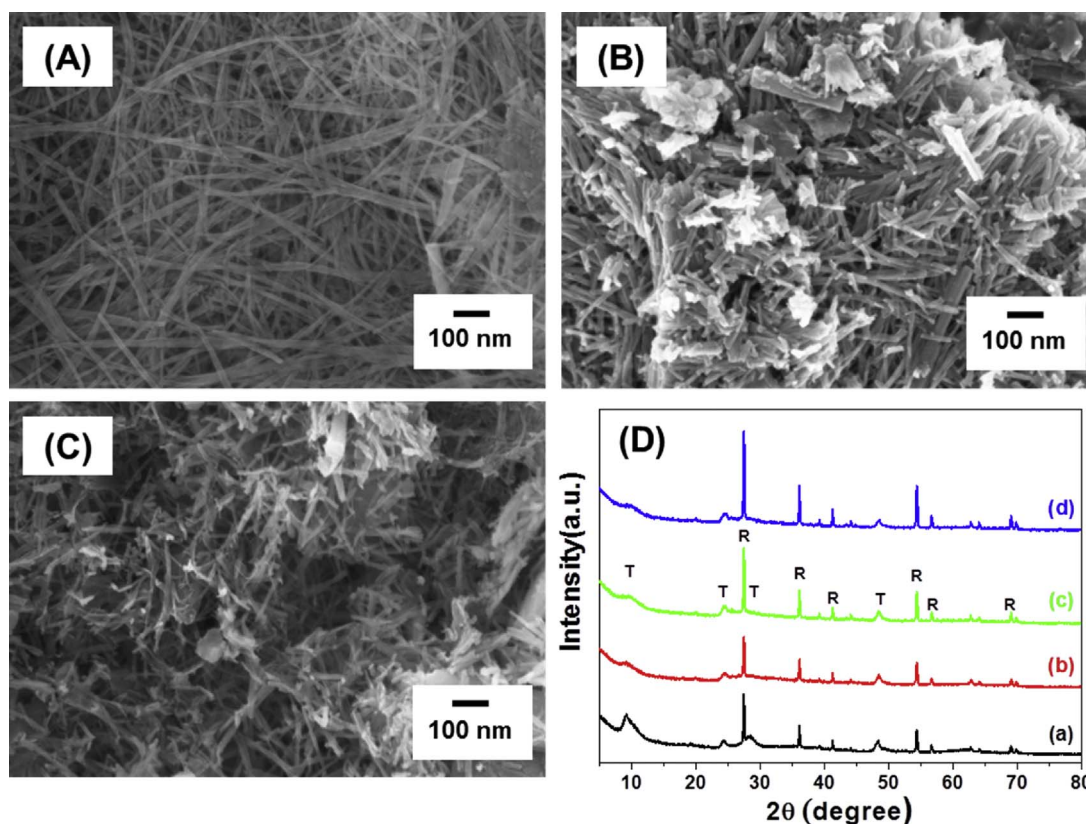
Fig. 4. FE-SEM images of (A) RS-TONR/TiNT-2D-0.5M, (B) RS-TONR/TiNT-2D-1M, and (C) RS-TONR/TiNT-2D-2M; and XRD patterns of (a) RS-TONR/TiNT-2D-0M, (b) RS-TONR/TiNT-2D-0.5M, (c) RS-TONR/TiNT-2D-1M, and (d) RS-TONR/TiNT-2D-2M (R: rutile, T: titanate).

nanorod and Titanate nanotube (RS-TONR/TiNT) composite photocatalyst was synthesized by a hydrothermal method for different reaction times. However, the RS-TONR/TiNT sample did not show any photocatalytic activity for the degradation of Orange (II) dye under visible light irradiation. To enhance the photocatalytic activity, acid treatment and Cu_xO loading on the surface of sample (RS-TONR/TiNT sample) was performed. TiO_2 nanoparticle with anatase phase was observed after calcination of Cu loaded RS-TONR/TiNT (Cu-TNP/TiNT/RS-TONR) sample. The overall photocatalytic activity was improved for Cu-TNP/TiNT/RS-TONR. The untreated RS-TONR/TiNT sample showed higher adsorption activity for Cd^{2+} ions. The 1.0 M HCl treated and 3 wt% copper oxide loaded sample showed excellent photocatalytic activity in the presence of cadmium ions. This enhanced result suggests that Cu3-TNP/TiNT/RS-TONR sample has great potential for simultaneous environmental removal of cadmium ion and dye pollutants.

2. Experimental procedure

2.1. Chemical reagents

All chemical reagents were used without further purification. Na_2HPO_4 (Kanto Chemicals, 99%), NaCl (Junsei Chemicals, 99.5%) and P25 (Degussa), $RhCl_3·3H_2O$ (Kojima, 99%), Sb_2O_3 (Acros, 99%), NaOH (Samchun, 98%), $Cu(NO_3)_2·3H_2O$ (Junsei, 99%) and Orange (II) sodium salt (Aldrich, 85%) were purchased. HCl (Assay 35%, Junsei Japan) acid was diluted with deionized (DI) water (CBNU, pH 7) in 25% acid-to-water volume ratio.

2.2. Synthesis and modification of Rh-Sb co-doped TiO_2 NR/titanate nanotube

Rh and Sb co-doped TiO_2 nanorod (RS-TONR) was prepared by molten salt flux method. In a typical procedure, P25 (Degussa), NaCl,

and Na_2HPO_4 (in 1:4:1 ratio, respectively) were ground together with rhodium (1 at%) and antimony (2 at%) precursors in a mortar pestle. The homogeneous mixture was then calcined inside a box furnace at 825 °C for 8 h. The calcined mixture was filtered with an excessive amount of boiled DI water to remove salts, and the filtrate was dried overnight at 80 °C in oven.

Further, the dried RS-TONR sample was synthesized in a one-pot hydrothermal method. The desired 0.7 g amount of RS-TONR was stirred up to 1 h in 70 mL of 10 M NaOH aqueous solution. Then the mixture solution was transferred to 125 mL Teflon hydrothermal reactor, and placed inside hot air oven at 160 °C, followed by different reaction time periods of 24 (1D), 48 (2D), and 72 (3D) h. The colored pulp type mixture was washed by centrifuge with DI water until the pH was 7.0. The collected wet sample was dried at 80 °C in hot air oven overnight. These samples hydrothermally synthesized for 1 day, 2 day, and 3 day are the mixture of rhodium and antimony doped nanorod (RS-TONR) and titanate nanotube (TiNT), and are here denoted as RS-TONR/TiNT-1D, RS-TONR/TiNT-2D, and RS-TONR/TiNT-3D.

The protonation of hydrothermally synthesized samples was followed by 0.3 g of RS-TONR/TiNT being dispersed in different concentrations (0.5, 1.0, and 2.0 M) of hydrochloric acid under continuous stirring for 3 h. The mixture was then washed with DI water, until the pH was 7.0. After filtration, the sample was dried in oven at 60 °C overnight. These acid treated samples are here denoted as RS-TONR/TiNT-0.5 M, RS-TONR/TiNT-1M, and RS-TONR/TiNT-2M, according to the different concentration of HCl.

The RS-TONR/TiNT-1M was used for copper oxide particles deposition by a wet impregnation method. In a typical experiment procedure, 0.25 g of protonated powder sample and a quantified amount of Cu_xO concentration (2, 3, 4, and 5 wt%) precursor solution was ground together with 3 mL ethyl alcohol. During grinding, excess amount (two times) of the solvent was allowed to evaporate. Finally, dry sample was calcined at 300 °C for 2 h inside the box furnace. After copper loading,
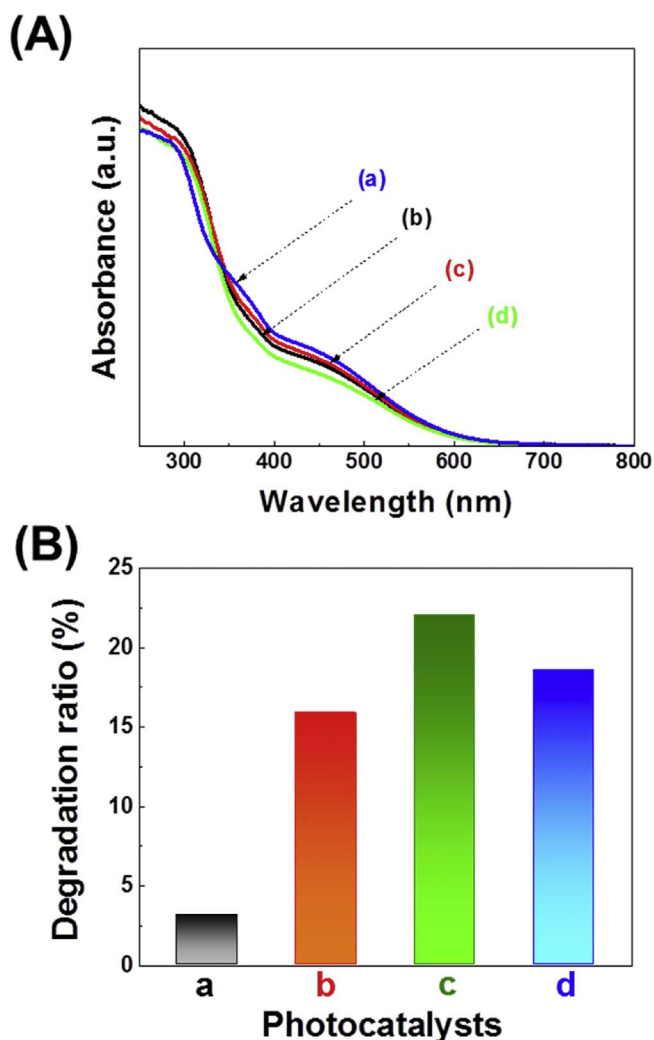
(A)

(B)

Fig. 5. (A) UV–vis DRS spectrum, and (B) photodegradation of 25 μM orange (II) dye under 420 nm visible light for (a) RS-TONR/TiNT-2D-0M, (b) RS-TONR/TiNT-2D-0.5M, (c) RS-TONR/TiNT-2D-1M, and (d) RS-TONR/TiNT-2D-2M.

the as-prepared samples are mixtures of TiO_2 nanoparticle (TNP), rhodium and antimony doped nanorod (RS-TONR) and titanate nanotube (TiNT), and are denoted as Cu2-TNP/TiNT/RS-TONR, Cu3-TNP/TiNT/RS-TONR, Cu4-TNP/TiNT/RS-TONR, and Cu5-TNP/TiNT/RS-TONR, according to the concentration of copper oxide.

2.3. Photocatalytic activity and adsorption of cadmium

The photocatalytic activity reaction was carried out in a Pyrex glass vessel at atmospheric pressure and ambient temperature under visible light. In a typical experiment, 50 mg of desired sample was mixed in 45 mL of 25 μM aqueous Orange (II) dye under continuous magnetic stirring. First, the solution was stirred for 30 min under dark condition, to equilibrium adsorption between the catalyst and the dye solution. Then the reactor glass was exposed to Xenon arc lamp (Abet, Japan) for 5 h, by using 420 nm cutoff filter. The degradant dye mixture was filtered by syringe filter system (pore size 0.2 nm), and 1.5 mL of filtrate solution was analyzed by UV–vis spectrophotometer (Shimadzu UV-2600 UV–vis-spectrophotometer).

Then, the adsorption of cadmium was tested to the same condition of dye degradation as the solution of 25 μM aqueous Orange (II) and the different concentration of cadmium ions. However, the solution was directly exposed to the Xenon arc lamp for 150 min by using 420 nm cutoff filter. The 1.3 mL of adsorbed cadmium mixture was filtrated by

centrifuge. These supernatants were analyzed by inductively coupled plasma atomic emission spectroscopy (ICP).

2.4. Characterization

X-Ray diffraction (XRD) structural analysis was performed using a PANalyticalX'pert Pro MPD diffractometer equipped with a Cu Kα radiation source (wavelength $K_{\alpha 1}$ = 1.540598 and $K_{\alpha 2}$ = 1.544426 Å) operated at 40 kV, 30 mA, and at a scan rate of 0.03° 2θ s^{-1} and 2θ over an angular range of 5°–80°. Scanning electron microscopy (SEM) observation was carried out by field emission scanning electron microscopy (FESEM) (SUPRA 40VP, Carl Zeiss, Germany) Chonbuk National University, equipped with X-ray energy dispersive spectrometry (EDS). X-ray photoelectron spectroscopy (XPS, Thermo Scientific XPS spectrometer) equipped with a monochromatic Al K_{α} X-ray source (hv = 1,486.6 eV) was used to study the valence state and elemental quantification of samples. The surface area and pore characterization system were obtained by an ASAP2020 Micromeritics instrument. Transmission electron microscopy (TEM) was performed with a JEOL JEM-3100F transmission electron microscope operating at 200 kV. Fourier Transform Infrared Spectrometer (FT-IR) was performed using a Paragon 1000 spectrometer (PerkinElmer). TRPL imaging was performed using a confocal microscope (MicroTime-200, Picoquant, Germany). A single-mode pulsed diode laser (379 nm with ∼30 ps pulse width and ∼20 μW laser power) was used as an excitation source. A dichroic mirror (Z375RDC, AHF), a longpass filter (HQ405lp, AHF), a 150 μm pinhole, and an avalanche photodiode detector (PDM series, MPD) was used to collect emissions from the samples. Time-correlated single-photon counting technique was used to measure photoluminescence (PL) decay curves, as a function of time with a resolution of 32 ps. Exponential fitting for the photoluminescence decays was performed by iterative least-squares deconvolution fitting using the Symphotime-64 software.

3. Result and discussion

3.1. Effect of the hydrothermal reaction time

The high quality crystalline rhodium and antimony doped nanorod (RS-TONR) with the diameter of ca. 120 nm and the length of 1.5–5 μm was synthesized by a molten salt flux method (Fig. 1A(a)). In the present work, we focused on hydrothermal synthesis of RS-TONR/TiNT for different reaction times, by using RS-TONR as a starting precursor. In general, aqueous alkali (10 M NaOH) solution was used for hydrothermal synthesis of tubular titanate structures [10]. Fig. 1A(b–d) shows the FE-SEM images of hydrothermally synthesized samples for different reactions, 1D, 2D and 3D, respectively. Fig. 1A(b) shows the morphology of RS-TONR/TiNT-1D sample. The short length nanotubes were grown on the surface of TiO_2 nanorods. During the hydrothermal reaction, most of the TiO_2 nanorods were untransformed. Fig. 1A(d) shows the morphology of RS-TONR/TiNT-3D, almost TONRs transformed into TNTs. However, the morphology of RS-TONR/TiNT-2D observed the admixtures of both TiNT and TONR (Fig. 1A(c)). The length of as-grown nanotubes on the surface of RS-TONR/TiNT-2D was around c.a. 10–20 nm observed. Fig. 1B shows the formation mechanism of RS-TONR/TiNT corresponding to their morphologies.

Fig. 2A, shows XRD diffraction patterns of RS-TONR and RS-TONR/TiNT (1D, 2D and 3D) samples. The diffraction peaks of 2θ = 27.5°, 36.1° and 54.3° of RS-TONR sample correspond to (110), (101) and (211) crystal planes of the reported rutile phase (JCPDS card number 89-4202), respectively [16]. New characteristic peaks around 2θ = 9.25°, 24°, 28° and 48° were observed in RS-TONR/TiNT (1D, 2D and 3D), which corresponds to the reported titanate peaks (JCPDS card number 72-0148) [10]. However, some rutile peaks were still observed in RS-TONR/TiNT-2D sample, while it was almost disappeared in RS-TONR/TiNT-3D sample. These results indicated that the rutile phase of
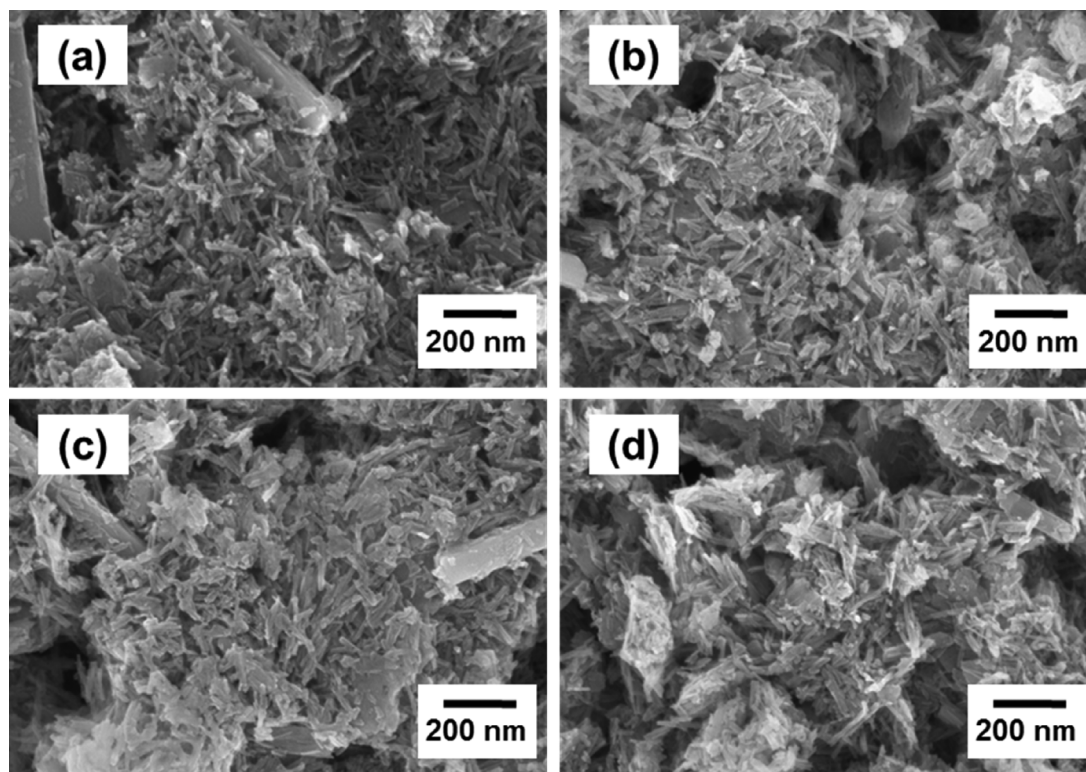
Fig. 6. FE-SEM images of (a) Cu2-TNP/TiNT/RS-TONR, (b) Cu3-TNP/TiNT/RS-TONR, (c) Cu4-TNP/TiNT/RS-TONR, and (d) Cu5- TNP/TiNT/RS-TONR.

RS-TONR was gradually transformed into titanate phase after the hydrothermal reaction, and RS-TONR/TiNT-2D sample consisted of mixed phase of RS-TONR and TiNT.

Fig. 2B shows the absorbance spectra of RS-TONRs and RS-TONR/TiNT (1D, 2D and 3D) samples. The absorbance onset of RS-TONR (deep orange color) sample was observed around 680 nm in the visible light region [31]. An absorbance shoulder was observed near 450 nm assigned to Rh^{3+} rhodium species. [6] The rhodium dopant species (Rh^{3+}) was responsible for absorbance in the visible light region and photocatalytic activity. [6] But the absorbance of the RS-TONR/TiNT decreased around the visible light region according to the increase in hydrothermal reaction times. This decrement in absorbance indicated that, might be RS-TONR/TiNT-3D composite loose the co-dopant property during hydrothermal reaction. And the amount of RS-TONR in RS-TONR/TiNT composite, which absorbs visible light, was decreased.

Fig. S1 shows the pore size distribution and nitrogen adsorption-desorption isotherm of RS-TONR/TiNT. Fig. S1A shows adsorption-desorption isotherm profile is type IV with H_3 hysteresis loop, and observed in the relative pressure (P/P_0) range of 0.7–1.0 [32]. The average pore diameters of RS-TONR/TiNT samples were observed as 17, 21 and 23 nm for TNT-1D, 2D and 3D samples, respectively. BET surface area for RS-TONR/TiNT samples is summarized in Table S1. RS-TONR/TiNT-2D sample shows the large specific surface area as ca. 131.1 m^2/g, in comparison with 1D and 3D samples.

The photocatalytic activity of RS-TONR and hydrothermally synthesized RS-TONR/TiNT (1D, 2D and 3D) samples were compared with the degradation of Orange (II) dye. The 25 µM Orange (II) dye was mixed with 50 mg photocatalyst, and this mixture was stirred for 30 min under dark condition, and then exposed to visible light ($\lambda \geq 420$ nm) irradiation for 5 h. Fig. 3A represents the photocatalytic performance of dye degradation from the as-synthesized and 1.0 M HCl-treated RS-TONR/TiNT samples. Initially, the untreated samples did not show significant photocatalytic activity. After the acid treatment, the RS-TONR/TiNT samples showed enhanced photocatalytic activity (Fig. 3A). Among all the RS-TONR/TiNT samples, the higher

photocatalytic degradation efficiency was around 23%, which was observed for 1.0 M HCl-treated RS-TONR/TiNT-2D sample. These results indicate that RS-TONR/TiNT-2D enhanced the photocatalytic activity after protonation (acid treatment). That is, the photocatalytic activity of the untreated RS-TONR/TiNT-2D sample was hindered, due to the presence of sodium ions that remained on its surface [16]. Fig. S3 shows the EDAX data of before and after acid treatment of RS-TONR/TiNT-2D sample. The acid treatment removes most of the sodium ions on its surface, which leads to enhanced photocatalytic activity of the other hydrothermally synthesized (RS-TONR/TiNTs) samples.

3.2. Effect of acid treatment concentration

To understand the effect of acid treatment, Fig. 4A–C shows the FE-SEM images of acid treated RS-TONR/TiNT-2D samples at different concentrations of 0.5, 1.0, and 2.0 M HCl, respectively. For a low concentration of acid treatment, RS-TONR/TiNT-2D retains the same morphology of nanotube. But at higher concentration of HCl, short and thick nanotubes are observed. In addition, 2.0 M HCl treated sample is transformed into irregular fragments and nanoparticles. These images confirm that the grain size and crystallinity are affected by high concentration of HCl [16]. Fig. 4D shows the corresponding XRD pattern of the acid-treated samples. The rutile peaks of samples treated with different concentrations of HCl showed almost the same pattern when compared to that of the RS-TONR/TiNT-2D sample [15]. However, a small increment in rutile peaks intensity was observed on increasing the acid concentration from 0.5 to 2.0 M, and the titanate characteristic peak of around 9.25° gradually disappeared. These results indicated that high acid concentration may lead to destruction of layered titanate nanostructure (collapsed walls of titanate), and change in phase of nanostructure [22].

Fig. S4 shows the nitrogen adsorption-desorption isotherms and the pore volume distribution BET surface areas of RS-TONR/TiNT-2D samples, treated with different concentrations of HCl. The N_2 adsorption-desorption isotherms follow similar type-IV with H_3 hysteresis
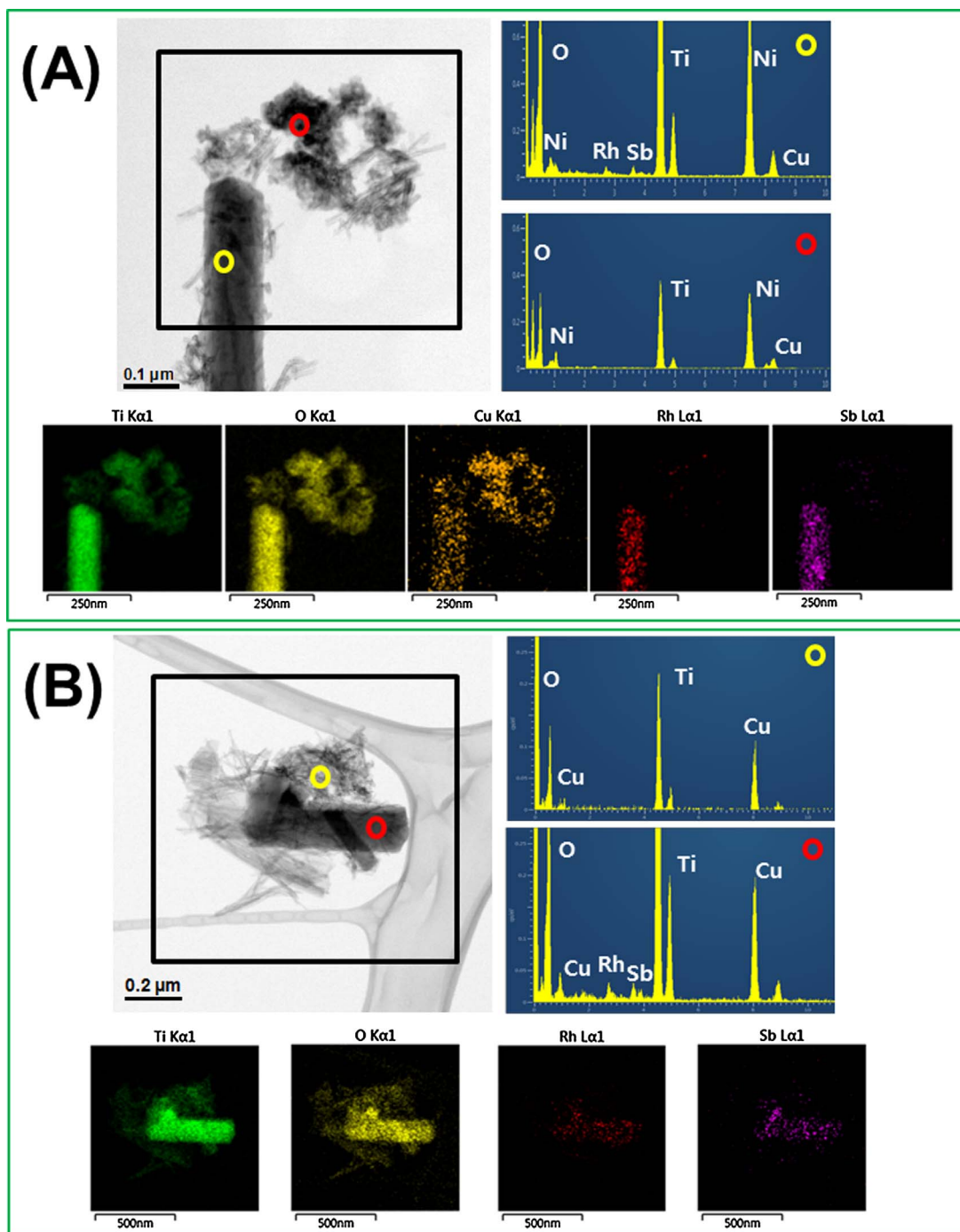
Fig. 7. TEM image and mapping of (A) Cu3-TNP/TiNT/RS-TONR, and (B) RS-TONR/TiNT-2D-1M.

loop, as shown in the untreated sample (Fig. S4A) [33]. The pore diameter for 1.0 M HCl treated (2.99 nm) sample is less than that of 0.5 M HCl treated (3.09 nm) sample. The surface area of acid-treated samples decreased with increasing concentration of HCl. The surface area for RS-TONR/TiNT-2D-1M sample was observed to be 172 m^2/g. Table S2 shows the BET surface area, pore size distribution, and pore volume data of acid treated RS-TONR/TiNT-2D samples.

Fig. 5A shows the UV–vis DRS spectra of RS-TONR/TiNT-2D samples treated with different concentrations of HCl. The sample treated with higher concentration (2.0 M HCl) shows slightly decrement around 450 nm wavelength than the untreated RS-TONR/TiNT-2D sample. However, different concentrations (0.5, 1.0 and 2.0 M) of acid treatment didn't show any significant effect on absorbance profile of

samples.

To study the effect of acid treatment over RS-TONR/TiNT-2D samples, the photocatalytic degradation of Orange (II) dye was performed under visible light irradiation (λ ≥ 420 nm). Fig. 5B shows that, among all samples RS-TONR/TiNT-2D-1M sample revealed the highest photocatalytic activity. The low (0.5 M) and high (2.0 M) concentrations acid treated sample showed very low photocatalytic activity. This result indicated that the surface charge of synthesized material affected by the pH of acid treatment. [16] The dye degradation efficiency around 23% was observed for RS-TONR/TiNT-2D-1M sample. In particular, RS-TONR/TiNT composite appears to offer effective photoactivity for dye degradation, because of its suitable band alignment with RS-TONR and TiNT. TiNT sample did not generate electron-hole pairs under visible
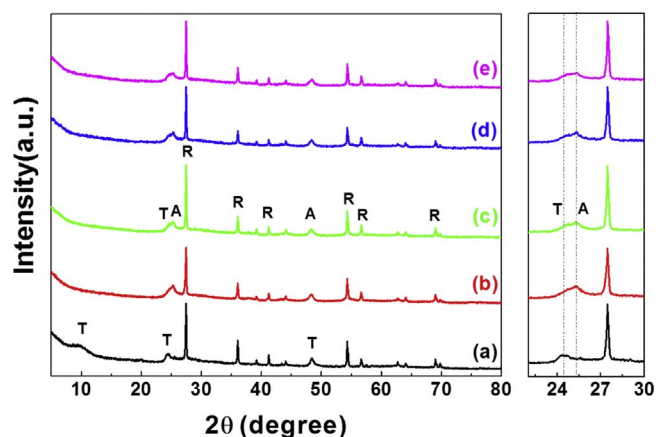
Fig. 8. XRD patterns of (a) Cu2-TNP/TiNT/RS-TONR, (b) Cu3-TNP/TiNT/RS-TONR, (c) Cu4-TNP/TiNT/RS-TONR, and (d) Cu5-TNP/TiNT/RS-TONR (R: rutile, A: anatase, T: titanate).

light irradiation [34,35]. However, RS-TONR/TiNT-2D facilitates the photo-induced charge transfer from the conduction band of RS-TONR to that of TiNT, as shown in Fig. 3B. Rhodium can modify the electronic properties of RS-TONR by introducing impurity energy levels between its valence band (VB) and conduction band (CB), respectively. These levels can also act as trap centers for electrons and holes, respectively, which substantially prevent charge recombination (Fig. 3B) [14].

3.3. Effect of Cu_xO loading on RS-TONR/TiNT

Fig. 6 shows FE-SEM images of different concentrations copper oxide loaded RS-TONR/TiNT-2D-1M samples, which are denoted as Cu-TNP/TiNT/RS-TONR. The effects of copper oxide loading were observed as broken structures and shortened tubular morphologies, compared to without copper oxide RS-TONR/TiNT-2D-1M sample. This result indicated that the high amount loading of copper oxide (2, 3, 4 and 5 wt%) leads to collapse of the nanotube structure into nanoparticle during the calcination process.

Fig. 7A and B, shows the TEM images of both without and with copper oxide loaded samples, respectively, that were analyzed to confirm the morphological change. Fig. 7A of the copper-loaded sample confirms that the sample contains three distinguishable nanostructures named as TiO_2 nanorod (Rutile), titanate nanotube, and TiO_2 nanoparticle (Anatase). According to TEM image mapping, TiO_2 nanoparticles of the collapsed titanate are also not doped by rhodium and antimony. Copper elements are located on titanate nanotube and TiO_2 nanoparticle. These results confirm that copper ions are exchanged into the interlayer of titanate nanotubes during the loading process. Meanwhile, the TEM image of RS-TONR/TiNT-2D-1M indicates that titanate nanotube is not doped by rhodium and antimony during the hydrothermal reaction process (Fig. 7B). As a result, the samples hydrothermally synthesized for different reaction times have an admixture of RS-TONR and titanate nanotube (TiNT). Even though, these admixtures of RS-TONR and titanate nanotube are observed for all samples, and samples are denoted as RS-TONR/TiNT.

Fig. 8 shows the XRD patterns of the Cu-TNP/TiNT/RS-TONR samples. In these samples, most characteristic peaks of titanate
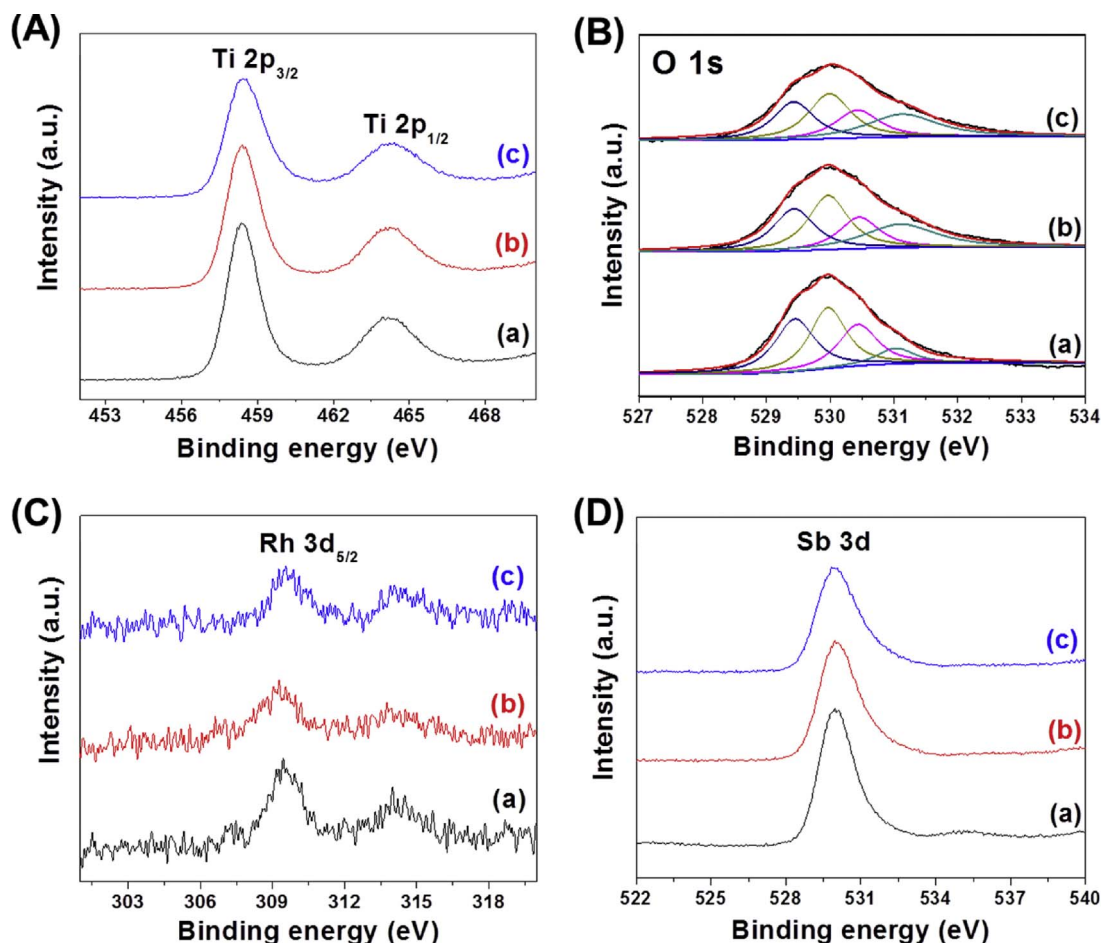

Fig. 9. XPS spectra of (A) Ti 2p, (B) O 1s, and (C) Rh 3d, and (D) Sb 3d; for (a) RS-TONR/TiNT-2D, (b) RS-TONR/TiNT-2D-1M, and (c) Cu3-TNP/TiNT/RS-TONR.
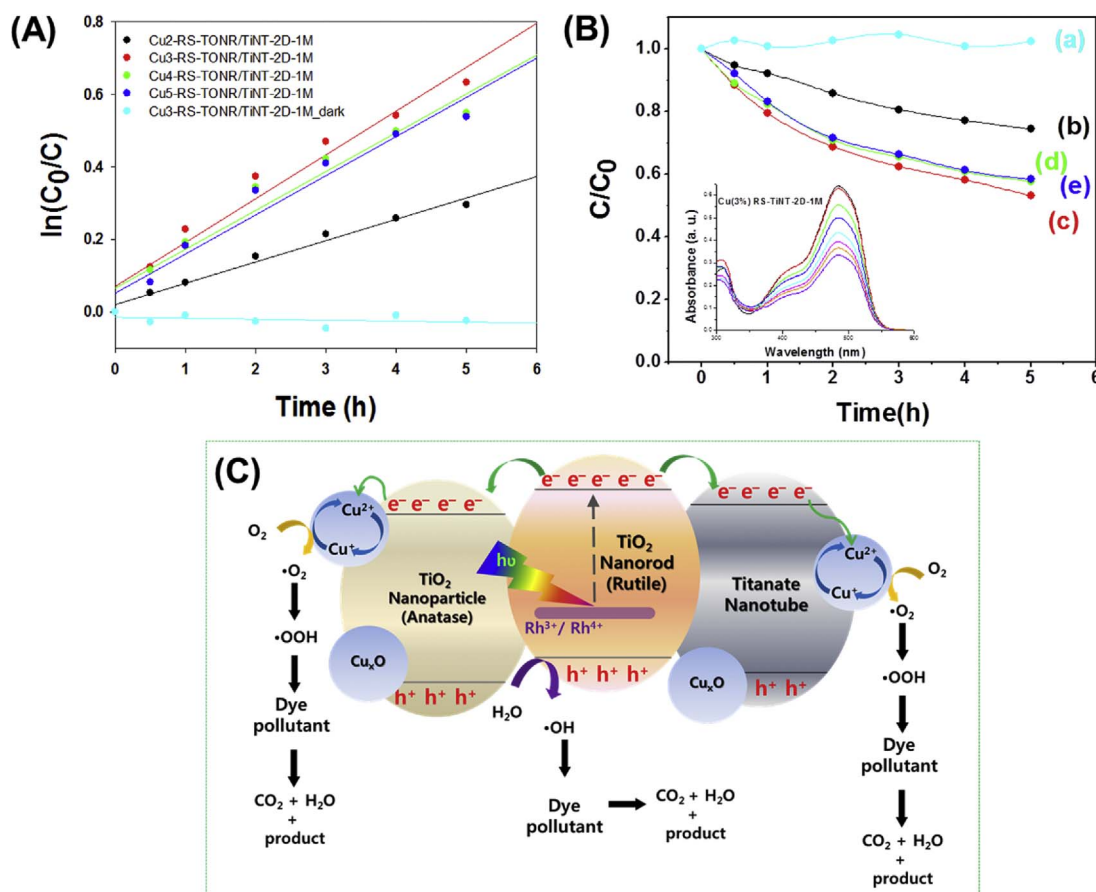
Fig. 10. The kinetics of photodegradation and (B) the photodegradation of 25 μM Orange (II) dye under 420 nm visible light for (a) Cu2-TNP/TiNT/RS-TONR, (b) Cu3-TNP/TiNT/RS-TONR, (c) Cu4-TNP/TiNT/RS-TONR, (d) Cu5-TNP/TiNT/RS-TONR, (e) Cu3-TNP/TiNT/RS-TONR dark condition; and (B) Diagram of the mechanism for Cu3-TNP/TiNT/RS-TONR.

nanotube have disappeared, and diffraction peaks of TiO_2 are observed after copper oxide loading. The characteristic peaks around 25° could come from the overlapped peaks of titanate and TiO_2 (anatase). These results indicate that the peaks of TiO_2 (anatase) in composite material occur during thermal transformation of the sample [36]. However, titanate nanotube has not perfectly changed to anatase phase of TiO_2.

A further XPS measurement was conducted to analyze the elemental composition and the oxidation state of each element in the as-synthesized materials. Fig. 9 shows the high resolution XPS spectra of Ti 2p, O 1s, Rh 3d and Sb 3d elements of RS-TONR/TiNT-2D, RS-TONR/TiNT-2D-1M, and Cu3-TNP/TiNT/RS-TONR, respectively. The Ti 2p peak contains doublet peaks at the binding energies of around 458.36 and 464.16 eV, which correspond to the Ti $2p_{3/2}$ and Ti $2p_{1/2}$ peaks, respectively (Fig. 9A) [37]. Doublet separation of Ti $2p_{3/2}$ and Ti $2p_{1/2}$ peaks is observed at 5.8 eV. The peak at 458.36 eV is a feature peak of Ti−O bond [14]. The oxygen O 1s XPS peak, corresponds to the binding energy ~530.01 eV, composed of four distinct oxygen components, which are denoted as O1, O2, O3 and O4 respectively, as shown in Fig. 9B. The O1 peak of around 531.04 eV as the binding energy represents the oxygen bonding with carbon atoms, which is further increased by acid treatments, as shown in Fig. 9B(b–c) [38–40]. The O2 oxygen peak around 530.45 eV as the binding energy represents the hydroxyl group (OH). The peak intensity of OH is decreased by acid treatment, which indicates that HCl removes the surface sodium ions of RS-TONR and TiNT that contain atmospheric adsorbed hydroxyl groups. During the acid treatment process, these sodium ions are easily detached from the surface of RS-TONR and TiNT, which decreases the peak intensity of OH. This decrement in the concentration of OH group is also verified by the FTIR analysis, as shown in Fig. S7. The O4 and O3 peaks around 529.44 and 529.96 eV represent the metallic bonding of

oxygen in Ti-O bond and defects of RS-TONR and TiNT, respectively. Fig. 9C,D shows the XPS spectra of rhodium and antimony elements, respectively. The rhodium peak (Rh 3d) contains doublet peaks around 308.84 and 313.44 eV, which represent the Rh $3d_{5/2}$ and Rh $3d_{3/2}$ state of Rh spin orbit [41,42]. However, the antimony peak around 529.96 eV is almost similar for all samples, and represents the Sb3d energy state. This result confirms that the Rh and Sb dopants coexist in the TiO_2 crystal lattice. The Sb dopant plays an important role in charge compensation with the co-dopant of Rh ions [6].

The dependence of photocatalytic degradation for Orange (II) dye was investigated on the amount of copper oxide loading on Cu-TNP/TiNT/RS-TONR sample. The Fig. 10A represents the plot of $\ln(C_0/C)$ versus time for photocatalytic degradation of Orange (II) dye by different concentration of copper oxide loaded Cu-TNP/TiNT/RS-TONR samples. In this system, reaction rate was fitted by pseudo-first-order reaction model that present in Table S3.

$$\ln(C_0/C) = kt \qquad (1)$$

where C_0 and C are the initial concentration of dye absorbance and reaction concentration of dye absorbance. These slopes of each plot were calculated and used to obtain the first-order rate constants (k). The dye degradation constants presented from the slope of the plots of $\ln(C_0/C)$ versus are used in order to have more precise comparison of the photocatalytic activity. The logarithmic plots were suggested the reaction kinetics of photodegradation of Orange (II) dye with the first-order reaction model. The rate constant of Cu3-TNP/TiNT/RS-TONR-2D-1M was calculated to 0.121 min^{-1} that was high value compared to other copper loaded samples. Fig. 10B shows the photocatalytic activity increased with the amount of copper oxide up to 3 wt%, and then decreased gradually with further increase of the amount of copper
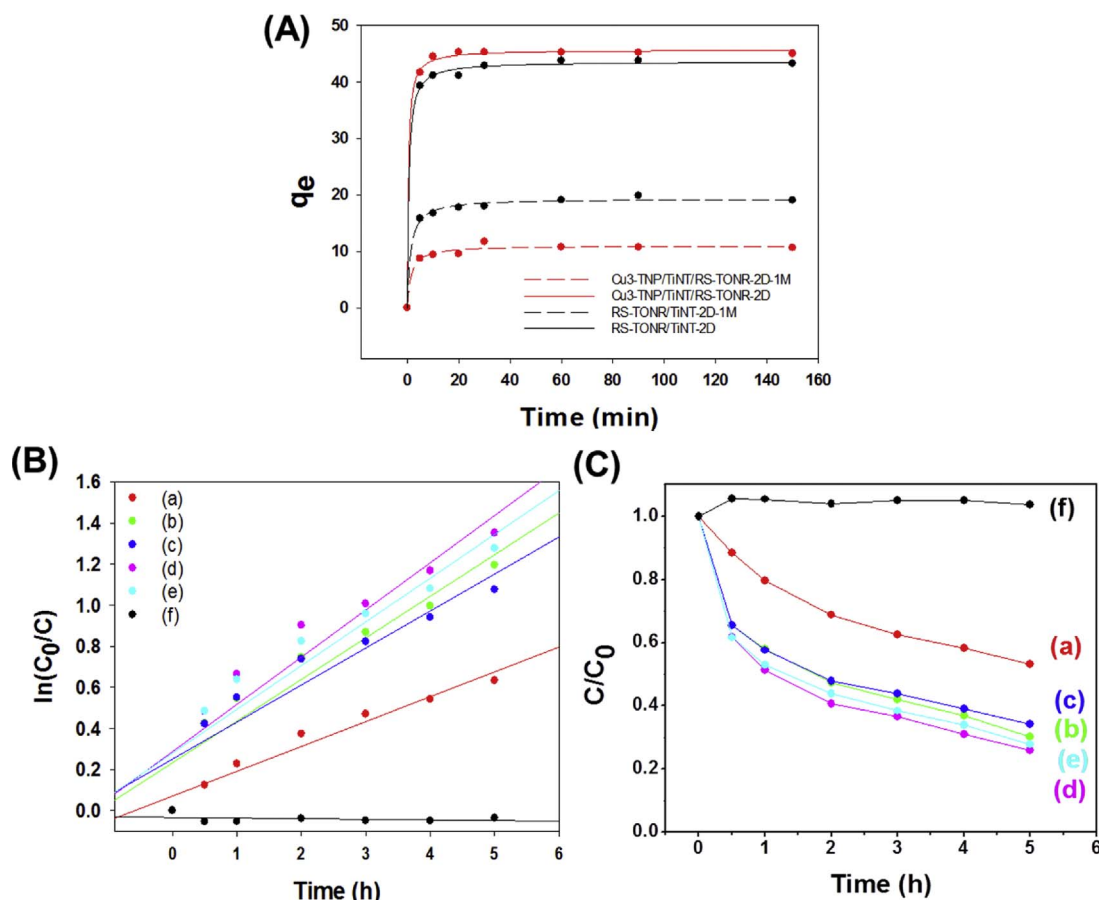
Fig. 11. (A) The adsorption of 25 µM orange (II) dye and cadmium under 420 nm visible light for RS-TONR/TiNT-2D, RS-TONR/TiNT-2D-1M, without acid treated Cu3-TNP/TiNT/RS-TONR, and Cu3-TNP/TiNT/RS-TONR [Cd: 50 ppm]; and (B) the kinetics and (C) the photodegradation of 25 µM orange (II) dye under 420 nm visible light for Cu3-TNP/TiNT/RS-TONR at different cadmium concentrations (a) [Cd: 0 ppm], (b) [Cd: 10 ppm], (c) [Cd: 25 ppm], (d) [Cd: 50 ppm], (e) [Cd: 100 ppm], and (f) [Cd: 50 ppm] under dark..
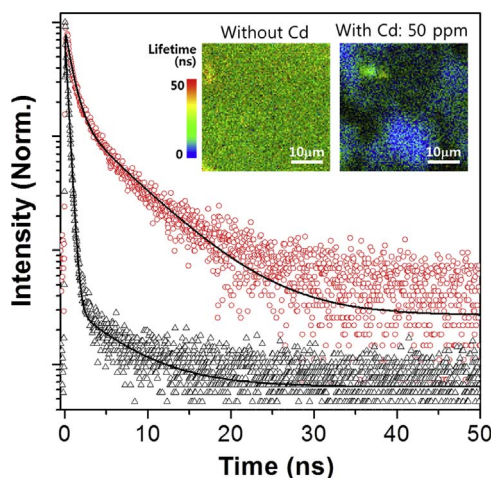

Fig. 12. Photoluminescence decays of Cu3-TNP/TiNT/RS-TONR (circle) and Cu3-TNP/TiNT/RS-TONR [Cd: 50 ppm] (triangle). The solid curves are fitted lines. The excitation wavelength is 379 nm. Inset is the TRPL images of the corresponding PL decays, which clearly present the faster lifetime after Cd adsorption.

Table 1
PL lifetime parameters of the catalysts before and after Cd adsorption.

Sample	A$_1$ (%)	τ$_1$ (ns)	A$_2$ (%)	τ$_2$ (ns)	$< \tau >$ (ns)
Cu3-TNP/TiNT/RS-TONR	82	0.87	18	6.15	4.08
Cu3-TNP/TiNT/RS-TONR [Cd: 50 ppm]	99	0.32	1	5.91	0.69

$I(t) = A_1 e^{-t/\tau_1} + A_2 e^{-t/\tau_2}$; $I(t)$ is the time-resolved photoluminescence intensity, A is the amplitude as a normalized percentage, and τ is the photoluminescence lifetime. Averaged lifetime, $< \tau >$, is defined by, $< \tau > = \sum_i A_i \tau_i^2 / \sum_i A_i \tau_i$ [55].

degradation for Orange (II) dye. In this figure, the photoelectrons are generated from the sub-band consisting of Rh 4d orbitals (Rh^{3+}/Rh^{4+}) to the conduction band consisting of Ti 3d orbitals in the RS-TONR under visible light irradiation. Most of the photo-excited electrons in the conduction band of RS-TONR transfer towards the conduction band of TiO$_2$ nanoparticle and titanate nanotube, due to the position of their band gap energy [43]. Finally, these photogenerated electrons could react with Cu^{2+} in the lattice of Cu$_x$O nanoparticle as shown in Fig. 10C, and then the Cu$^+$ in Cu$_x$O nanoparticle are formed by photoreduction. These Cu$^+$ ions are further oxidized into Cu(II) species by transferring electrons to the oxygen molecules. Meanwhile, the electrons of oxidized species are shared towards oxygen molecules to form reactive oxygen species (ROS), such as the superoxide anion radicals (·O$_2^-$). Moreover, the photogenerated holes are contributed to generate hydroxyl radicals from surface water. Superoxide and hydroxyl radicals can attack the targeted dye pollutant to be degraded as CO$_2$, H$_2$O and less harmful products [30].

loading, showing a maximum activity of 47% at 3 wt%. In general, when the photon energy of incident light is higher than the band gap energy of the semiconductor, electro-hole pairs are generated. Fig. 2 shows that the RS-TONR absorbs the visible light region. But, TiNT and TiO$_2$ NP are wide-band gap materials that show absorbance in the UV light region [34,35].

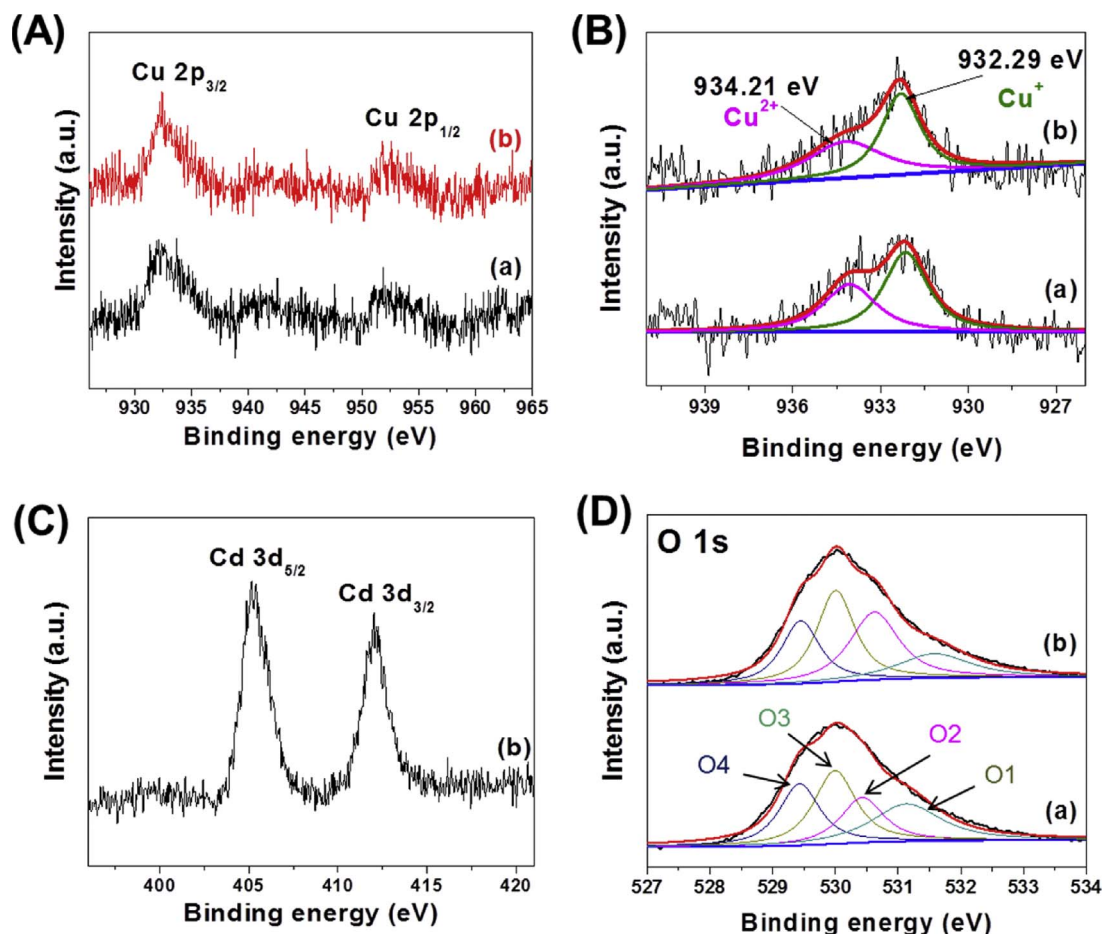Fig. 10C shows the general mechanism of photocatalytic

Fig. 13. XPS high resolution spectra of (A) Copper, (B) Fitted Cu 2p$_{3/2}$ peaks, and (C) Cadmium (D) oxygen, for (a) Cu3-TNP/TiNT/RS-TONR, and (b) Cu3-TNP/TiNT/RS-TONR [Cd: 50 ppm].

3.4. Simultaneous removal of toxic metal ions and dye

Fig. 11A shows the adsorption isotherm curve for simultaneous removal of Orange (II) dye and cadmium ion under visible light irradiation. Cd ions are added into the Orange (II) dye solution, and the concentration of Cd ions is detected by Inductively Coupled Plasma Spectrometry (ICP) during photocatalytic reaction. During this reaction process, the concentration of Cd^{2+} ion is fixed as 50 ppm, and mixed together with Orange (II) dye (25 μM) solution. The acid treated Cu3-TNP/TiNT/RS-TONR sample shows a very low adsorption capacity of Cd^{2+} ion of 10 ppm. However, no acid-treated Cu3-TNP/TiNT/RS-TONR sample shows a high adsorption capacity of Cd^{2+} ion. This high adsorption activity of untreated sample indicates the ion-exchange mechanism [10]. Untreated sample contains sodium ions that actively participate in the ion-exchange process. The low adsorption capacity of the acid-treated sample also indicates that H$^+$ protons in the interlayer of titanate nanotube could exchange with Cd^{2+} ions in the adsorption reaction [18]. To understand the effect of copper oxide towards the Cd^{2+} ion adsorption, both acid-treated and untreated RS-TONR/TiNT sample was used for ion exchange reaction. However, acid treated RS-TONR/TiNT-2D-1M sample shows a higher (20%) adsorption capacity than that of Cu3-TNP/TiNT/RS-TONR sample, but untreated RS-TONR/TiNT-2D sample shows less adsorption capacity than Cu3-TNP/TiNT/RS-TONR sample.

To compare the photocatalytic activity of Orange (II) dye at different concentration Cd^{2+}, the slope of the plots of ln(C$_0$/C) *versus* time are shown in Fig. 11B. The logarithmic plots were suggested the reaction kinetics of photodegradation of Orange (II) dye with the first-order reaction model. Fig. 11B shows the synergistic effect of Cu$_x$O loading

and cadmium ions for the photocatalytic degradation of Orange (II) dye. The concentration of cadmium ion changes according to fixed concentration of Orange dye (25 μM) solution during photocatalytic reaction. After adding the cadmium, the rate constant of Cu3-TNP/TiNT/RS-TONR-2D was enhanced. A higher efficiency of photocatalytic dye degradation over Cu3-TNP/TiNT/RS-TONR sample is observed (around 75%) in the presence of 50 ppm cadmium ions under visible light irradiation. However, this sample does not show any photocatalytic activity under dark condition. This result indicates that the photocatalytic activity of Cu3-TNP/TiNT/RS-TONR sample is boosted by the visible light.

The photocatalytic efficiency of photocatalyst highly depends on photo-excited charge carrier density in the spatially separated localized trap states for further consecutive photo-reduction and/or photo-oxidation processes. In order to achieve the higher density of charge carriers in localized catalytic sites, separately, rather than direct recombination of electron-hole pair to photon, rapid non-radiative trapping to the catalytic sites is inevitably beneficial right after photo-excitation [44,45]. Fig. 12 shows PL decay curves of the hybrid photocatalysts before and after Cd adsorption. The measured time-resolved PL curves are well fitted by two-exponential decay model. The Cu3-TNP/TiNT/RS-TONR is composed of short-lived and long-lived lifetime components. The short-lived component becomes dominant in the 50 ppm Cd adsorbed catalyst, while the long-lived component negligibly contributes. The calculated averaged PL lifetime ($< \tau > = 4.08$ ns) of the Cu3-TNP/TiNT/RS-TONR is dramatically reduced by 83.1% ($< \tau > = 0.69$ ns) after adsorption of Cd component (Table 1). This indicates 5.9 times faster decay rate and increased contribution of non-radiative processes in the Cd adsorbed catalyst.

This dramatic quenching can be assigned to the multiple pathways of photogenerated electron trapping to TiNT, TNP and metallic and oxidized form of Cd component. Therefore, it is noteworthy to mention that the significant contribution of the non-radiative trapping pathways is critical to localize charge carriers and higher catalytic efficiency in this hybrid catalyst system.

Moreover, the efficiency of photogenerated charge separation over Cu3-TNP/TiNT/RS-TONR sample is enhanced due to the surface deposited Cd^{2+} ions. The Cadmium species is adsorbed and then deposited on the surface of Cu3-TNP/TiNT/RS-TONR sample by photoreduction during photocatalytic reaction [46,47]. Fig. 13B shows the Cd 3d peaks around 405.1 and 412.0 eV correspond to the binding energies of Cd $3d_{5/2}$ and Cd $3d_{3/2}$ of metallic cadmium [48]. However, the binding energy of Cd $3d_{5/2}$ peak in metallic Cd is very similar to those of CdO, Cd(OH)$_2$, respectively [48–50]. Therefore, we will investigate it in the next work with a specific analysis tool. In the previous reported work, the photoreduction mechanism of Cd^{2+} ions is well described, which is similar to our experimental results [46,51]. Cadmium ion adsorbed on the surface of photocatalyst can be reduced in a sequential two-electron transfer reaction from its conduction band. Also, the metallic Cd increased the hydroxyl groups during the photoreduction process [29]. This increase of hydroxyl groups is confirmed by the XPS spectra of O 1s peak, which is indicated in Fig. 13C.

Fig. 13A shows the high resolution XPS spectra of Cu 2p of samples prepared before and after the photocatalytic reaction for simultaneous Cd^{2+} ion and dye removal. The XPS spectra of Cu 2p contain two peaks around 932.4 and 952.5 eV, which correspond to the Cu $2p_{3/2}$ and Cu $2p_{1/2}$ states, respectively [32]. The existence of shake-up peaks indicates the presence of Cu^+ and Cu^{2+} [52,53]. Further, it is deconvoluted to confirm the existence of mixed Cu species of the Cu $2p_{3/2}$ peak (Fig. 13B). The higher intensive peak located around 932 eV corresponds to the Cu^+. Another peak located around 934 eV comes from the oxidation state of Cu^{2+} [54].

In summary, we have evaluated the simultaneous removal of heavy metal and Orange (II) dye, and enhanced the photocatalytic activity of dual phase RS-TONR/TiNT composite. Cu$_x$O loading and Cd^{2+} ion adsorption showed a synergistic effect for photocatalytic dye degradation. This clean approach using visible light and photocatalyst is very convenient for environmental applications (Fig. 13).

4. Conclusions

In this study, we studied the simultaneous removal of Orange (II) dye and cadmium ions by using Cu$_x$O loaded mixed phase TiO$_2$ codoped with rhodium and antimony (Cu3-TNP/TiNT/RS-TONR). The RS-TONR/TiNT was hydrothermally synthesized for different reaction times, with RS-TONR as the precursor material. The RS-TONR/TiNT samples did not show any photocatalytic activity, even though they can absorb visible light. Improved activity was observed after acid treatment with 1.0 M HCl. Among samples treated with different concentration of HCl, RS-TONR/TiNT-2D showed the highest photocatalytic activity. Further, the photocatalytic activity of this material was further enhanced after copper oxide loading. This means that Cu3-TNP/TiNT/RS-TONR sample generates the ROS species ($\cdot O_2$, $\cdot OOH$) in the presence of oxygen. The concentration of Cu3-TNP/TiNT/RS-TONR composite shows the best photocatalytic performance. Moreover, the simultaneous removal of Orange dye and cadmium ions over Cu3-TNP/TiNT/RS-TONR showed higher photocatalytic activity, because of the synergistic effect of Cu$_x$O loading and Cd^{2+} ion adsorption. This enhanced result suggests that the as-synthesized sample has great potential for environmental treatment by an eco-friendly method.

Acknowledgments

Appendix A. Supplementary data

Supplementary data associated with this article can be found, in the online version, at http://dx.doi.org/10.1016/j.apcatb.2017.11.013.

References

[1] C.W. Lai, S. Sreekantan, J. Nanomater. 2011 (2011) 7.
[2] J. Choi, H. Park, M.R. Hoffmann, J. Phys. Chem. C 114 (2010) 783–792.
[3] H. Kato, A. Kudo, J. Phys. Chem. B 106 (2002) 5029–5034.
[4] J. Kuncewicz, B. Ohtani, Chem. Commun. 51 (2015) 298–301.
[5] F.E. Oropeza, R.G. Egdell, Chem. Phys. Lett. 515 (2011) 249–253.
[6] R. Niishiro, R. Konta, H. Kato, W.J. Chun, K. Asakura, A. Kudo, J. Phys. Chem. C 111 (2007) 17420–17426.
[7] Y. Hou, X. Li, X. Zou, X. Quan, G. Chen, Environ. Sci. Technol. 43 (3) (2009) 858–863.
[8] T. Li, X. Li, Q. Zhao, Y. Shi, W. Teng, Appl. Catal. B 156–157 (2014) 362–370.
[9] J. Pan, X. Li, Q. Zhao, T. Li, M. Tade, S. Liu, J. Mater. Chem. C 3 (2015) 6025.
[10] L.K. Dhandole, J. Rye, J.M. Lim, B.T. Oh, J.H. Park, B.G. Kim, J.S. Jang, RSC Adv. 6 (2016) 98449–98456.
[11] W. Liu, T. Wang, A.G.L. Borthwick, Y. Wang, X. Yin, X. Li, J. Ni, Sci. Total Environ. 456–457 (2013) 171–180.
[12] H. Zhang, L. Cao, W. Liu, G. Su, Appl. Surf. Sci. 259 (2012) 610–619.
[13] W. Liu, A.G.L. Borthwick, X. Li, J. Ni, Microporous Mesoporous Mater. 186 (2014) 168–175.
[14] M.T.N. Le, B.K. Lee, RSC Adv. 6 (2016) 31347–31350.
[15] W. Liu, A.G.L. Borthwick, X. Li, J. Ni, Microporous Mesoporous Mater. 186 (2014) 168–175.
[16] L.K. Dhandole, M.A. Mahadik, S.G. Kim, H.S. Chung, Y.S. Seo, M. Cho, J.H. Ryu, J.S. Jang, ACS Appl. Mater. Interfaces 9 (28) (2017) 23602–23613.
[17] A.R. Khataee, M.B. Kasiri, J. Mol. Catal. A: Chem. 328 (2010) 8–26.
[18] L. Xiong, C. Chen, Q. Chen, J. Ni, J. Hazard. Mater. 189 (2011) 741–748.
[19] G. Sheng, S. Yang, J. Sheng, D. Zhao, X. Wang, Chem. Eng. J. 168 (2011) 178–182.
[20] X. Zhao, Z. Cai, T. Wang, S.E. O'Reilly, W. Liu, D. Zhao, Appl. Catal. B 187 (2016) 134–143.
[21] H.Y. Niu, J.M. Wang, Y.L. Shi, Y.Q. Cai, F.S. Wei, Microporous Mesoporous Mater. 122 (2009) 28–35.
[22] C.K. Lee, S.S. Liu, L.C. Juang, C.C. Wang, M.D. Lyu, S.H. Hung, J. Hazard. Mater. 148 (2007) 756–760.
[23] W. Chu, Water Res. 35 (2001) 3147–3152.
[24] F.C. Wu, R.L. Tseng, J. Hazard. Mater. 152 (2008) 1256–1267.
[25] Z.R. Holan, B. Volesky, I. Prasetyo, Biotechnol. Bioeng. 41 (1993) 819–825.
[26] B. Volesky, H. May, Z.R. Holan, Biotechnol. Bioeng. 41 (1993) 826–829.
[27] K.H. Chong, B. Volesky, Biotechnol. Bioeng. 47 (1995) 451–460.
[28] B. Benguella, H. Benaissa, Water Res. 36 (2002) 2463–2474.
[29] T. Wang, W. Liu, N. Xu, J. Ni, J. Hazard. Mater. 250–251 (2013) 379–386.
[30] R. Doong, S. Chang, C. Tsai, Appl. Catal. B 129 (2013) 48–55.
[31] B. Liu, H.M. Chen, C. Liu, S.C. Andrews, C. Hahn, P. Yang, J. Am. Chem. Soc. 135 (2013) 9995–9998.
[32] H. Yu, J. Yu, B. Cheng, J. Lin, J. Hazard. Mater. 147 (2007) 581–587.
[33] J. Huang, Y. Cao, Q. Huang, H. He, Y. Liu, W.G.M. Hong, Cryst. Growth Des. 9 (2009) 3632–3637.
[34] S. Guo, H. Ning, M. Li, R. Hao, Y. Luan, B. Jiang, RSC Adv. 5 (2015) 13011–13015.
[35] A.T. Vu, Q.T. Nguyen, T.H.L. Bui, M.C. Tran, T.P. Dang, T.K.H. Tran, Adv. Nat. Sci.: Nanosci. Nanotechnol. 1 (2010) 015009–015013.
[36] H.K. Seo, G.S. Kim, S.G. Ansari, Y.S. Kim, H.S. Shin, K.H. Shim, E.K. Suh, Sol. Energy Mater. Sol. Cells 92 (2008) 1533–1539.
[37] R.A. Doong, C.Y. Liao, Sep. Purif. Technol. 179 (2017) 403–411.
[38] J. Zhang, X. Liu, R. Blume, A.H. Zhang, R. Schlogl, D.S. Su, Science 322 (2008) 73–77.
[39] C. Hontorialucas, A.J. Lopezpeinado, J.D.D. Lopezgonzalez, M.L. Rojascervantes, R.M. Martinaranda, Carbon 33 (1995) 1585–1592.
[40] A. Bagri, C. Mattevi, M. Acik, Y.J. Chabal, M. Chhowalla, V.B. Shenoy, Nat. Chem. 2 (2010) 581–587.
[41] E.N.K. Glover, S.G. Ellington, G. Sankar, R.G. Palgrave, J. Mater. Chem. A 4 (2016) 6946–6954.
[42] L.S. Kibis, A.I. Stadnichenko, S.V. Koscheev, V.I. Zaikovskii, A.I. Boronin, J. Phys. Chem. C 120 (2016) 19142–19150.
[43] Z. Xiong, X.S. Zhao, J. Am. Chem. Soc. 134 (2012) 5754–5757.
[44] Z. Bian, T. Tachikawa, W. Kim, W. Choi, T. Majima, J. Phys. Chem. C 116 (48) (2012) 25444–25453.
[45] H.W. Jeong, W.S. Chae, B. Song, C.H. Cho, S.H. Baek, Y. Park, H. Park, Energy Environ. Sci. 9 (10) (2016) 3143–3150.
[46] C.R. Chenthamarakshan, H. Yang, Y. Ming, K. Rajeshwar, J. Electroanal. Chem. 494 (2000) 79–86.
[47] V.N.H. Nguyen, R. Amal, D. Beydoun, Chem. Eng. Sci. 58 (2003) 4429–4439.
[48] A.J. Du, D.D. Sun, J.O. Leckie, J. Hazard. Mater. 187 (2011) 401–406.

[49] J. Moulder, W. Stickle, P. Sobol, K. Bomben, J. Chastain (Ed.), Handbook of XrayPhotoelectron Spectroscopy, Perkin-Elmer Corporation, Minnesota, 1992.

[50] H. Khallaf, C.T. Chen, L.B. Chang, O. Lupan, A. Dutta, H. Heinrich, A. Shenouda, L. Chow, Appl. Surf. Sci. 257 (2011) 9237–9242.

[51] P. Chowdhury, S. Athapaththu, A. Elkamel, A.K. Ray, Sep. Purif. Technol. 174 (2017) 109–115.

[52] M. Jung, J. Scott, Y.H. Ng, Y. Jiang, R. Amal, Int. J. Hydrogen Energy 39 (2014)

12499–12506.

[53] M. Lei, N. Wang, L. Zhu, Q. Zhou, G. Nie, H. Tang, Appl. Catal. B 182 (2016) 414–423.

[54] K. Lalitha, G. Sadanandam, V.D. Kumari, M. Subrahmanyam, B. Sreedhar, N.Y. Hebalkar, J. Phys. Chem. C 144 (2010) 22181–22189.

[55] J.R. Lakowicz, Principles of Fluorescence Spectroscopy, Springer, New York, 2006.